J Mater Sci: Mater Electron (2017) 28:10747–10757
DOI 10.1007/s10854-017-6851-4

$La_{0.5}Sm_{0.5}FeO_3$: a new candidate for magneto-electric coupling at room temperature

M. G. A. Ranieri[1] · M. Cilense[1] · E. C. Aguiar[3] · A. Z. Simões[2] · M. A. Ponce[4] · E. Longo[1]

Received: 16 December 2016 / Accepted: 25 March 2017 / Published online: 6 April 2017

Abstract Samarium substituted lanthanum orthoferrite $La_{0:5}Sm_{0:5}FeO_3$ thin film has been prepared by soft chemical method. A single perovskite phase with orthorhombic crystallographic structure was attained. Magnetic and ferroelectric orderings of the film is observed at room temperature (RT). The magnetization of the sample measured at room temperature increases non-linearly with the increase of magnetic field, which suggests the presence of dipole–dipole/exchange interaction in the sample. The resistivity measured in the temperature range 25–375 °C showed that the film is a semiconducting material with low resistivity. The Cole–Cole model reveals different grain boundaries electrical resistance caused by the equilibrium concentration of oxygen vacancies in orthoferrite and that the addition of samarium results in loss of oxygen during sintering. The ferroelectric behaviour of $La_{0:5}Sm_{0:5}FeO_3$ at RT is also confirmed by its capacitance–voltage (*C*–*V*) characteristic suggesting a weak ferroelectric behaviour at room temperature. The variation of dielectric constant as a function of frequency predicts the presence of spontaneous polarization in the sample. The semiconductor electrical behavior of the $La_{0:5}Sm_{0:5}FeO_3$ is mainly composed of tunneling current.

✉ A. Z. Simões
alezipo@yahoo.com

[1] Laboratório Interdisciplinar em Cerâmica (LIEC), Departamento de Físico-Química, Instituto de Química, UNESP, Araraquara, SP CEP: 14800-900, Brazil

[2] Faculdade de Engenharia de Guaratinguetá, Universidade Estadual Paulista- Unesp, Av. Dr. Ariberto Pereira da Cunha, 333, Bairro Pedregulho, Guaratinguetá, SP CEP: 12516-410, Brazil

[3] Universidade Estadual de Mato Grosso do Sul, Cidade Universitária, Caixa Postal 351, Dourados, MS CEP: 79804-970, Brazil

[4] Instituto de Investigaciones en Ciencia y Tecnología de Materiales (INTEMA) (CONICET-Universidad Nacional de Mar del Plata), Juan B. Justo 4302, 7600 Mar del Plata, Argentina

1 Introduction

Most of the ferroelectrics and multiferroic materials are the oxide perovskites with general stoichiometry ABO_3, which normally applies to the mineral $CaTiO_3$. In the materials with perovskite structure, the small cations 'B' are at the centre of an octahedron of oxygen anions and the large cations 'A' are at the unit cell corners [1, 2]. The high value of the local internal electric field produces the spontaneous polarization leading to the on-set of ferroelectric ordering and the angles between the connecting lines made by cation B oxygen cation B are nearly 180, which induces superexchange interaction leading to the on-set of magnetic ordering in the same system. Many compounds having the structure similar to ABO_3 crystallize with the orthorhombic distortion in the perovskite structure and $LaFeO_3$ (LFO) is the prototype of this series [1]. The crystal structures of these materials are derived from the standard cubic structure through the distortion of the BO_6 octahedral [3]. The perovskites are of particular interest for their relatively simple crystal structure with many diverse properties viz., magnetic, piezoelectric, optical, catalytic and dielectric. In our recent work [4], we have shown that LFO exhibited *p*-type conduction (i.e., the holes were the dominant charge carriers). But the room temperature magnetization of this material is not high enough. To overcome this limitation, we have prepared thin films of $La_{0.5}Sm_{0.5}FeO_3$ on platinum coated silicon substrates. Magnetization of the film

has been measured and has been considerably enhanced in the $La_{0.5}Sm_{0.5}FeO_3$. Electric and dielectric properties have been investigated which indicates that the present sample is ferroelectric. Interestingly, the antiferromagnetic insulator (LFO) becomes a semiconducting material with substantially enhanced magnetic properties after the 50% replacements of La by Sm ion. High-quality nanocrystalline rare earth orthoferrites, especially $LnFeO_3$ (Ln = a lanthanide element), have drawn much attention because of their unique physical and chemical properties for various applications [5]. Most ferroelectrics and multiferroic materials are oxide perovskites with a general stoichiometry ABO_3. In perovskite structured materials, the small cations (B) are at the centre of an octahedron of oxygen anions and the large cations (A) are at the unit cell corners. The high local internal electric field produces spontaneous polarization, leading to the onset of ferroelectric ordering. Further, the cation B-oxygen-cation-B angle is nearly 180°, which induces superexchange interaction, leading to the onset of magnetic ordering in the same system. Many compounds with the ABO_3 stoichiometry crystallize with an orthorhombic distortion in the perovskite structure and LFO is a prototype of this series. The crystal structures of these materials are derived from the standard cubic structure by the distortion of the BO_6 octahedral. These perovskites are of particular interest because of their relatively simple crystal structure in combination with excellent magnetic, piezoelectric, optical, catalytic, and dielectric properties [6].

$LaFeO_3$ is a perovskite oxide [7, 8], which has been extensively studied because of its potential applicability in gas sensors, electrodes of solid-state fuel cells, spin valves, and other exchange bias applications in magnetic memory, or for oxygen sensing [4, 7–15]. LFO with antiferromagnetic characteristics [9, 10] crystallizes in an orthorhombically distorted perovskite structure with lattice parameters $a = 5.557$ Å, $b = 5.5652$ Å, and $c = 7.8542$ Å [14]. The Néel temperatures of thin film and bulk LFO are as high as 670 and 740 K, respectively [10]. The antiferromagnetism and an extremely high ordering temperature (T_N) of LFO are very promising for its application in the storage industry, spin valves, exchange bias applications, and heterostructures of magnetic/magnetic and magnetic/electric films [11]. In this work, we have used a solution-based method widely used to prepare thin oxide films for the preparation of $La_{0.5}Sm_{0.5}FeO_3$ thin films. Solution-based preparation methodologies involve either sol–gel processing or decomposition of organometallics. Various types of sol–gel processing include colloidal sol–gel processing, synthesizing inorganic polymeric gels from organometallic compounds, and formation of an organic polymeric complex which originates the polymeric precursor method (PPM). PPM can involve [16–18] in situ polymerization of organometallic monomers or the preparation of a viscous solution containing metal ions, polymers, and a solvent. This viscous solution can be easily converted into a thermoplastic gel at high polymer concentrations. In situ PPM has been used extensively to obtain ceramic powders with small particles and a single phase [19].

This method was originally developed by Pechini [20] and is based on the chelation of a metallic cation by a carboxylic acid (such as citric acid) and further polymerization, which is promoted by the addition of ethylene glycol, leading to polyesterification. To obtain crack-free films, process parameters, including solution viscosity and ionic concentration, substrate-film adhesion, heating conditions, preparation atmosphere, substrate, and withdrawal speed need optimization. Differences between the thermal expansion coefficients of the film and the substrate also influence PPM [21, 22]. In this work, a single-phase film is prepared by the soft chemical method and its structural, dielectric, magnetic and multiferroic properties are investigated. Sm^{3+} ion is chosen a new candidate for the improvement of the multiferroic behaviour of LFO: (i) the enhancement of the magnetization and (ii) the increment of the dielectrical properties by increasing the value of the dielectric constant and decreasing the dielectric loss. To the best of our knowledge, no report on the structure, magnetic and dielectric properties and/or the multiferroic properties of samarium substituted LFO is found in the literature.

2 Experimental procedure

The $La_{0:5}Sm_{0:5}FeO_3$ (LFO:Sm) thin film were prepared by the PPM, as described elsewhere [23]. The precursor solutions of lanthanum and iron were prepared by adding and stirring the raw materials (La_2O_3 -J.T.Baker 99.5%, $FeC_6H_5O_7{\cdot}(NH_4)_2H\ C_6H_5O_7$)—Vetec 99.9%, $C_6H_8O_7{\cdot}H_2O$—Merck 99.5%, HNO_3—Merck 99.5%, $C_2H_6O_2$—Aldrich 99.5%. Sm_2O_3 (99.9% purity, Aldrich) in to ethylene glycol and concentrated aqueous citric acid under heating. Appropriate quantities of the solutions of La and Fe were mixed and homogenized by stirring at 90 °C. The molar ratio of metal: citric acid: ethylene glycol was 1:4:16. The viscosity of the resulting solution was set to 20 cP by adjusting the water content using a Brookfield viscometer. The films were spin-coated from the deposition solution onto a Pt (111)/Ti/SiO_2/Si substrate. The typical Platinum coated Silicon wafers have the following characteristics. (100) orientated Si substrate with a size of 100 mm × ~500 u thick has a SiO_2 0.5 µ deposited on both sides of wafer and TiO_2 400 ± 50 Å (Polished side) and Pt1500 ± 100 Å (Polished side) (Typical Pt resistivity: 15 µ Ohm-cm). Figure 1 illustrates the schematic representation of the substrate-film-top-electrode. The LFO:Sm

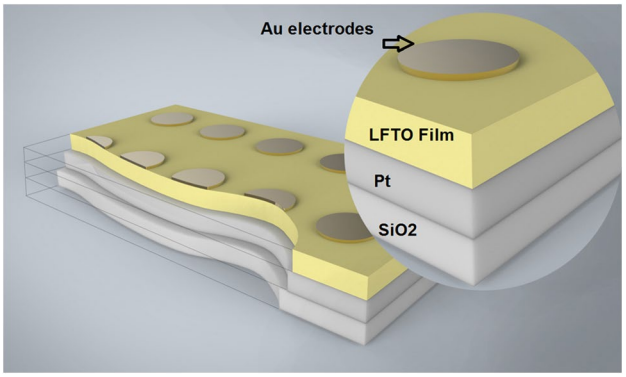

Fig. 1 Schematic representation of the substrate-film-top-electrode employed in this work

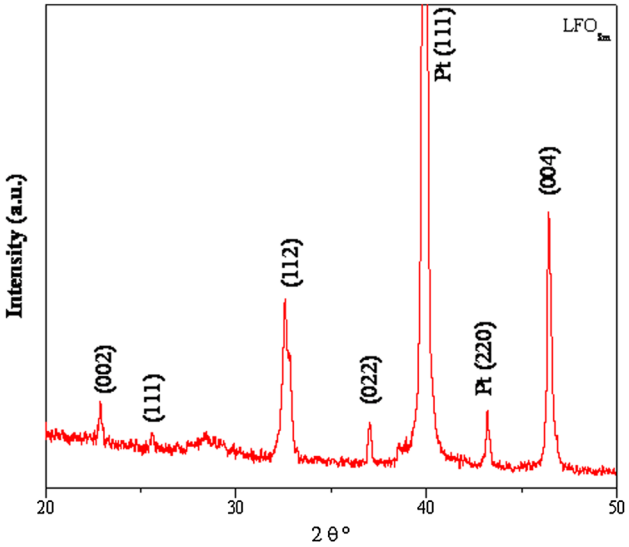

Fig. 2 X-ray diffraction patterns of the LFO:Sm thin films deposited on Pt/Ti/SiO_2/Si(100) substrates annealed at 500 °C for 2 h

films completely crystallized after annealing for 2 h at 500 °C. Multilayered films were obtained by spin-coating the deposition solution 10× on the surface of the substrate at 5000 rpm. The films were annealed at 300 °C for 1 h at a heating rate of 3 °C/min in a conventional furnace and later crystallized at 500 °C for 2 h in static air environment. The number of layers was set as a function of the desired thickness to achieve the desired electrical properties. The films were analyzed by X-ray diffraction (XRD) at room temperature (using a Rigaku-DMax 2000PC diffractometer) with Cu-Kα radiation in the 2θ range 20°–60° at 0.3 °/min. The crystallite size (d) of the films was calculated using the Scherrer equation $d = k\lambda/\beta \cos\theta$, where k is a constant, λ is the X- ray wavelength, and β is the full width at half maximum (FWHM) of the maximum reflection measured from a slow scan, and θ is the diffraction angle of the main peak. The thickness of the annealed films was measured using scanning electron microscopy (SEM, Topcom SM-300) by imaging the transverse section using backscattered electrons. Three measurements were acquired to obtain the average thickness, which was ~260 nm. The microstructural characterization of the films was carried out using transmission electron microscopy (TEM, Philips CM-20). For the TEM study the electron-transparent thin foils were prepared by mechanical thinning of the sintered samples followed by ion milling using argon ions at 3.5 kV which are inserted onto 300 mesh Cu grids. The surface morphology of the thin films was characterized by atomic force microscopy (AFM) in the tapping mode (Nanoscope IIIa-Bruker). For electrical measurements, a top Au electrode (0.5 mm in diameter) was sputtered through a shadow mask at room temperature. After the deposition of the top electrode, the film was annealed in a tube furnace under oxygen at 300 °C for 1 h to decrease the oxygen vacancies. The electrical properties of the capacitor (Au/LFO:Sm/Pt/Ti/SiO_2/Si) were measured on a Radiant Technology RT6000 A tester equipped with a micrometer probe station in a virtual ground mode at 60 Hz. The dielectric properties of the capacitor were measured with an HP4192A impedance/gain phase analyzer under zero bias at room temperature as a function of frequency in the range from 1 kHz to 1 MHz. The capacitance–voltage characteristic was measured in the metal-ferroelectric-metal (*MFM*) configuration using a small *AC* signal of 10 mV at 100 kHz. The *AC* signal was applied across the sample, while the *DC* was swept from positive to negative bias. Ferroelectricity was investigated using a Sawyer–Tower circuit attached to a computer controlled standardized ferroelectric test system (Radiant Technology 6000 A). Also, impedance measurements were performed with a frequency response analyser (HP 4192) with amplitude of 100 mV. The resistivity measurements were carried out from 150 to 300 °C by four probe technique PC-controlled four-probe direct current (DC). The magnetization measurements were carried out using a vibrating sample magnetometer (VSM, Quantum Design™). The electrical current density J) measurements were obtained in air using a PC-controlled four-probe direct current (DC) equipment. The thermopower was evaluated using K-thermocouples (which measured the applied temperature gradient) and platinum electrodes (which measured the resulting voltages).

3 Results and discussion

Figure 2 shows the XRD pattern of the LFO:Sm thin films deposited on Pt/Ti/SiO_2/Si(100) substrates annealed at 500 °C for 2 h. The film is fully crystallized since intense peaks are evident. Furthermore, with the exception of the Pt

(111) peaks, peaks corresponding to impurity phases, such as FeO and Fe_2O_3, were absent, indicating that single phase films were obtained by the chemical preparation used here. In addition, thermodynamically stable garnet ($Ln_3Fe_5O_{12}$) phases were absent in the XRD patterns, confirming the high purity of the products. This suggests that the annealing temperature can eliminate compositional fluctuations and the conversion of Fe^{3+} to Fe^{2+}, which influence the appearance of secondary phases. The most intense peak (100%) of LFO:Sm is observed at $2\theta = 46.4°$ for (004) plane with preferred orientation as a consequence of favorable matching of the atomic arrangements in LFO:Sm, and the underlying Pt planes. The diffraction peaks reveal a single perovskite phase with orthorhombic crystallographic structure matching with the indexed database (JCPDS file No. 74-2203) with lattice parameters (calculated from the XRD patterns) $a = 0.535 \pm 0.006$ nm, $b = 0.734 \pm 0.002$ nm, and $c = 0.512 \pm 0.008$ nm.

To confirm the thickness and surface morphology, surface and cross section FEG-SEM and TEM were carried out. Figure 3a shows that the film was composed of uniform fine grains, several tens of nm in dimensions. Distinct grain boundaries were absent, which may be related with the low leakage current density because the opening of grain boundaries is suggested to lead to an increase of such parameter (Fig. 3a). Low annealing temperatures may also contribute to the low leakage current density because annealing at high temperatures can produce many defects, which can result in high leakage. TEM analyses observation shows the formation of dense, uniform film. TEM clearly demonstrated the polycrystallinity of the grains in the plane of the films. The grains were uniformly shaped and the grain size estimated from the dark-field images was about 70 nm, Fig. 3a. Small pores (less than 10 nm in size) were present within the grains and along the grain boundaries. The small grains suggest suppression of oxygen vacancy concentration, which results in slower oxygen ion motion and consequently, lower grain growth rate. However, the grain boundaries were clearly distinguishable. Hence, the smaller grain size obtained can result from low crystallization temperatures because of the differences in the chemical bond strength between the Fe–O, La–O and Sm–O atoms. Further, the electron diffraction patterns indicated strong randomness in the atomic positions, as previously observed in the XRD results. Field emission scanning electron microscopy (FEG-SEM) image is also shown (Fig. 3b). Grains of about 35–45 nm are observed, which are similar in size to those reported from X-ray and FEG-SEM investigations (~47 nm). The method is suitable for the production of films up to ~700 nm thickness. An increase of the film thickness above 700 nm can cause cracking at the following thermal treatment. Preparation of thicker films requires a more complicated deposition

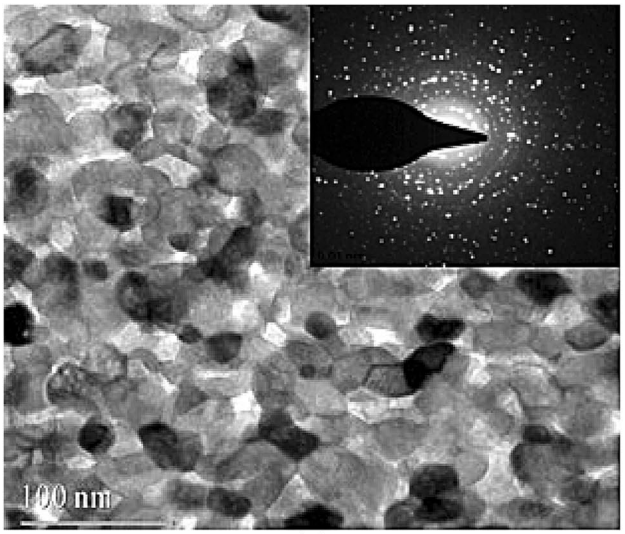

(a)

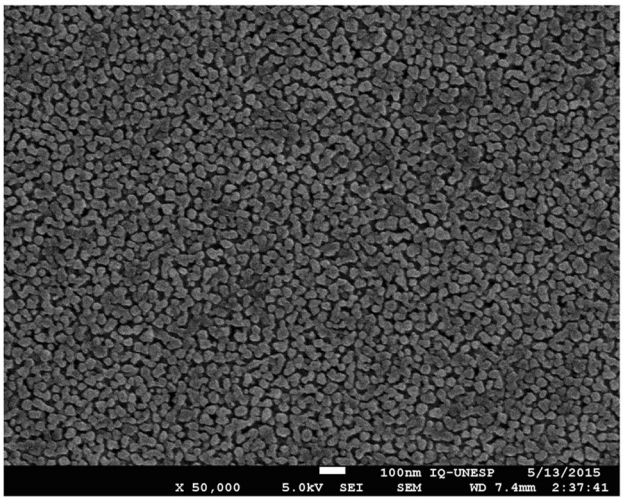

(b)

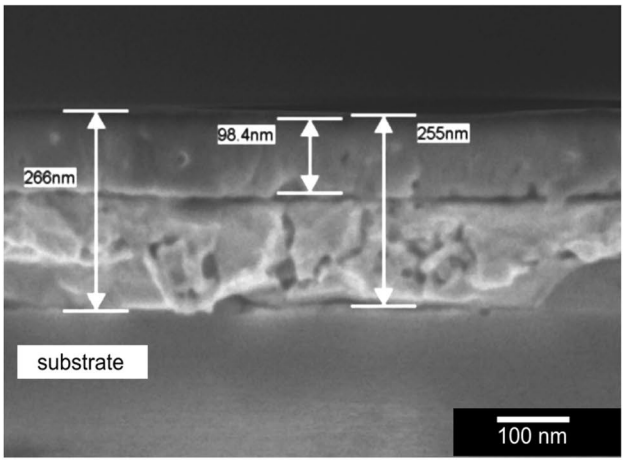

(c)

Fig. 3 **a** Transmission electron micrograph, **b** field emission scanning electron microscopy (FEG-SEM) and **c** cross section scanning electron microscopy images of the LFO:Sm thin films deposited on $Pt/Ti/SiO_2/Si(100)$ substrates annealed at 500 °C for 2 h

procedure. Moreover, the surface was compact and smooth and Fig. 3c indicates the film thickness to be about 256 nm.

Figure 4 depicts the surface morphology of the LFO:Sm films deposited on platinum coated silicon substrate. As show, the film surface has a homogeneous surface, with a rms surface roughness of 2.62 nm. Additionally, a uniform distribution of the flat surface was clearly observed, implying that the film grew by 2D nucleation process. Hence, the PPM allows for the preparation of LFO:Sm films with controlled morphology. The average grain size of 45 nm was measured. The PPM used in this study was found to be effective in improving the surface morphology of the film because the precursor film underwent optimized nucleation and growth process, resulting in films with a homogeneous and dense microstructure. In addition, the homogeneous microstructure of such films allowed for the application of a uniform voltage, which significantly affected the measured electrical properties can be applied uniformly onto it.

The dielectric permittivity and the dissipation factor of the films are presented in Fig. 5a. The dielectric measurements were carried out at room temperature as a function of frequency and the respective values were determined at 1 MHz by applying a small ac signal of 50 mV amplitude. The amplitude of applied signal was kept low to minimize the domain contribution so that the dielectric constant obtained does not regard polarization state in the material. As it can be seen, the film possess small dielectric dispersion at low frequency since at which the dielectric constants decrease slightly with the frequency. It means that the films has good interface between the LFO:Sm film and Pt bottom electrode. As shown, the dielectric constant shows very little dispersion with frequency indicating that our films possess low defect concentrations at the interface film-substrate. The low dispersion of the dielectric

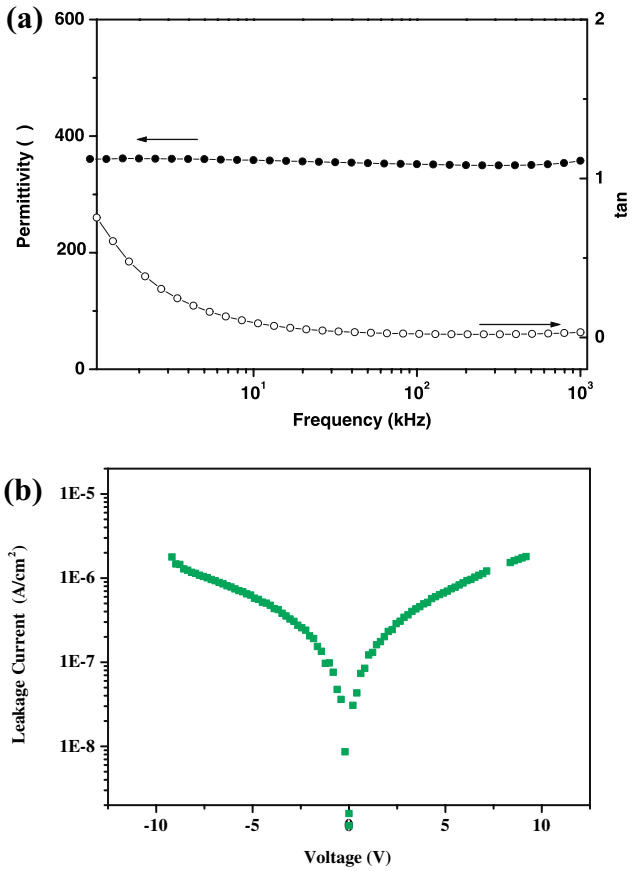

Fig. 5 **a** Dielectric permittivity and dielectric loss spectra as a function of frequency and **b** leakage current density versus applied voltage of the LFO:Sm thin films deposited on Pt/Ti/SiO_2/Si(100) substrates annealed at 500 °C for 2 h

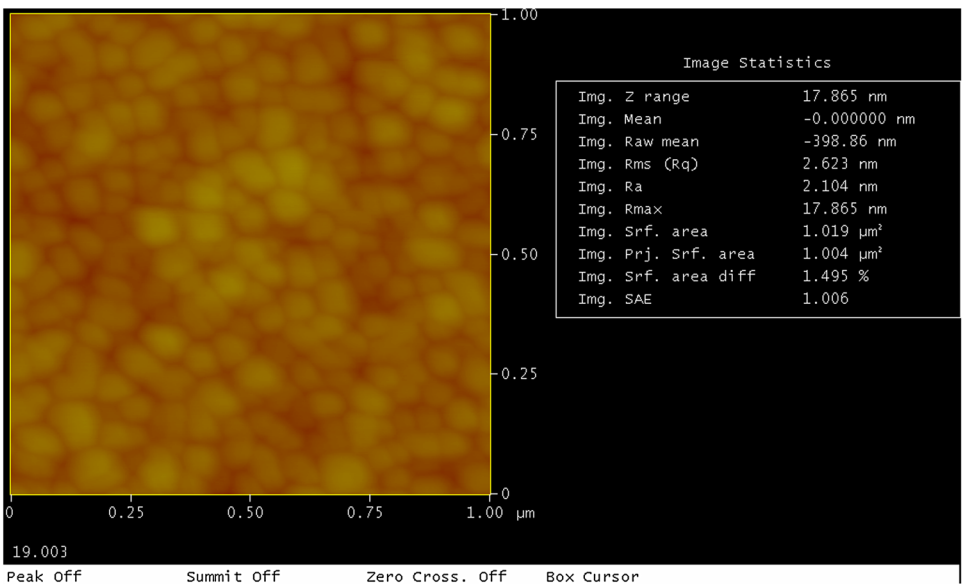

Fig. 4 Atomic force microscopy images of the LFO:Sm thin films deposited on Pt/Ti/SiO_2/Si(100) substrates annealed at 500 °C for 2 h

constant and the absence of any relaxation peak in tan δ indicate that both, interfacial polarization of the Maxwell Wagner type and a polarization produced by the electrode barrier can be neglected in the film. The dielectric constant and dissipation factor, at 1 MHz, were found to be 358 and 0.036, respectively. The LFO:Sm film had higher relative dielectric permittivity when compared with those previously reported films [4]. The observed behaviour of dielectric permittivity may be associated with significant effect on the overall microstructure of the system [24] and due to the ability to switch the electric dipoles with the frequency of the applied field. Figure 5b shows the leakage current density as a function of the voltage measured at room temperature. The curve was recorded with a voltage step width of 0.1 V and elapsed time of 1.0 s for each voltage. The measured logarithmic current density (log J) versus the voltage (V) is symmetric and shows two clearly different regions. The lower leakage current density of the LFO:Sm film may be attributed to the reduced number of electrons injected from the cathode at a rate faster than they can travel through the film. A low voltage was applied to overcome the larger repulsion forces caused by an increase in the amount of non-neutralized charges in the traps of the film. Since the conductivity is strongly affected by the characteristics of the film-electrode interface, the lower leakage current observed here may be probably attributed to differences in grain size, density, and lower stress in the plane of the film because of differences in the antiferromagnetic material and the interface. The current density increased linearly with the external voltage at low applied voltage, suggesting ohmic conduction. At higher field strengths, the current density increased exponentially, implying that at least a part of the conductivity originated from the Schottky or Poole–Frenkel mechanism. The leakage current density of the LFO:Sm films at 5.0 V was 10^{-7} A cm^{-2}.

It well known that currents in this materials depends on the barrier height and the depletion layer. By solving the Poisson's equation under the 'depletion approximation', or resorting to the Gauss theorem, the maximum grain-boundary barrier height for a spherical grain is given by

$$V_B = \frac{qN_D R^2}{6\epsilon} \quad (1)$$

where R is radius of the grain and N_D is the donor density. Based on reported experiments, for typical oxides semiconductors, Schottky barrier heights are around 1 eV and the donor density is in the order of 10^{24} m^{-3} [25, 26].

With these values, the critical grain size (diameter) for which the grains are completely depleted is ~110 nm. For LFO:Sm film, we will focus in studying if grains presented an overlapping of the depletion regions (with grains completely depleted). If so, the capacitances would be very small and the complex impedance analysis becomes with no sense. Then, in what follows we will focus in calculate the Schottky barrier heights and the donor density. Particularly, in our case, using the value of permittivity, we can estimate that complete depletion occurs for $N_d \leq 7 \times 10^{23}$ m^{-3}.

In order to study the electrical dependence with temperature, Impedance Spectroscopy (IS) measurements during cooling (from 200 to 150 °C) process were carried out (Fig. 6a). It is known that the electrical behavior of the semiconductors oxides films was analyzed using impedance plots in which the impedance Z is shown in a complex plane with the reactance, imaginary part of Z, plotted against the resistance, real part of Z [25]. The resulting circular forms suggest a parallel RC equivalent circuit. Figure 6b shows the equivalent circuit generally used to describe the impedance of polycrystalline semiconductors [27]. The proposed model consider the electrode, grain boundary, traps, and bulk equivalent elements. Deep bulk traps are represented with the incorporation of a R_t element in series with a typical *CPE*

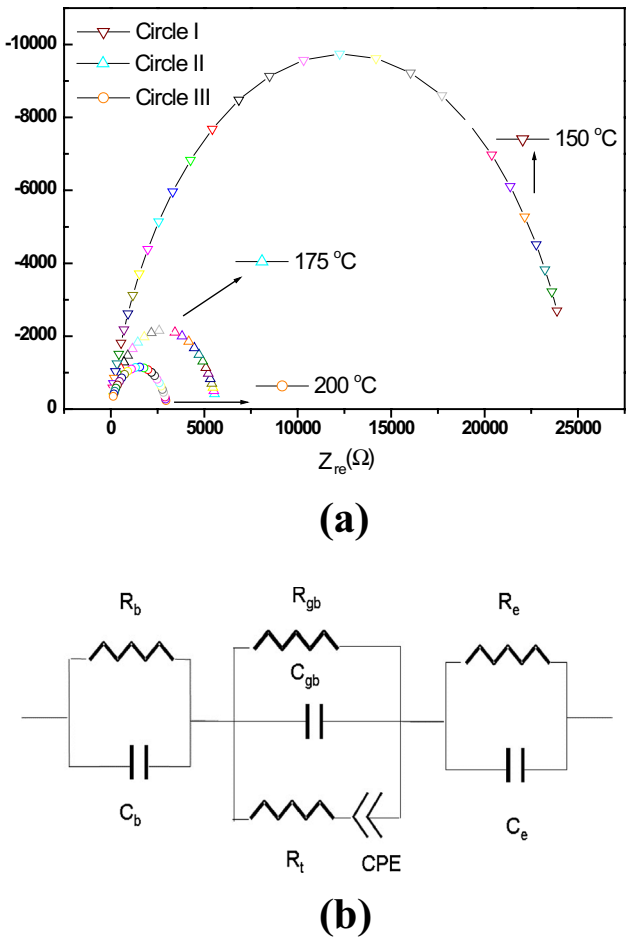

Fig. 6 **a** Cole–Cole plot of complex-impedance diagram in the temperature range 150–200 °C and **b** equivalent circuit of the LFO:Sm thin films deposited on Pt/Ti/SiO_2/Si(100) substrates annealed at 500 °C for 2 h film with temperature

circuit element. The capacitance C_{gb} and the resistance R_{gb} are associated with the intergrains and R_b with the bulk. The impedance of a resistance R_{gb} in parallel with a capacitance C is given by.

$$Z_{gb} = \frac{R_{gb}\frac{1}{j\omega C}}{R_{gb} + \frac{1}{j\omega C}} \tag{2}$$

that can be expressed as

$$Z_{gb} = \frac{R_{gb} - j\omega {R_{gb}}^2 C}{1 + \omega^2 {R_{gb}}^2 C^2} \tag{3}$$

From this equation the real part, Z_{gb}', and the imaginary part, Z_{gb}'', can be easily extracted and they are connected as

$${Z_{gb}}'^2 + {Z_{gb}}''^2 = R_{gb} Z_{gb}' \tag{4}$$

Equation (4) can be written as

$$(Z_{gb}' - R_{gb}/2)^2 + {Z_{gb}}''^2 = (R_{gb}/2)^2 \tag{5}$$

This is a circumference of radius $R_{gb}/2$ centered at $R_{gb}/2$. The addition of a series resistance R_b only shifts the resulting circle. Thus, R_b and R_{gb} are derived from the low- and high-frequency resistance, respectively, and the capacity can be found from the maximum value of the reactance.

The results illustrated in Fig. 6a reveal that the semi-circumferences become smaller as a function of temperature which indicates that R_{gb} is a monotonically decreasing function of temperature, effect that is expected since current transport mechanisms in semiconductor oxides are all temperature dependent. Also, the electrical behavior of the film at low frequencies can be better described with the electrical model shown in Fig. 6b, where, for the sake of simplicity, R_b is neglected. In this circuit, the resistance R_t and the capacitance C_t mimic the effect of deep traps. For the proposed equivalent circuit, Fig. 6b, the total conductivity (G_p) and total capacitance (C_p) can be expressed as follows:

$$G_p = \frac{1}{R_{gb}} + C_t \omega^2 \frac{\tau}{1 + \omega^2 \tau^2} \tag{6}$$

and

$$C_p = C_{gb} + C_t \frac{1}{1 + \omega^2 \tau^2} \tag{7}$$

where, $\tau = C_t R_t$ is the mean lifetime of the traps.

Based on the model of Fig. 6a, R_{gb} and C_{gb} can be determined from the conductance and capacitance values in the limits of very low and very high frequencies, respectively, *i.e.*

$$G_{tot}\big|_{\omega \to 0} = \frac{1}{R_{gb}} \tag{8}$$

and

$$C_{tot}\big|_{\omega \to \infty} = C_{gb} \tag{9}$$

Here, C_{gb} was measured at frequencies above 100 kHz and R_{gb} between 1 and 10^{-2} Hz (or also can be determinate using a DC multimeter).

The grain boundary capacitance can be also expressed as

$$\frac{1}{C_{gb}} = 2\left(\frac{2\varphi n^2}{q\epsilon_0 \epsilon_r N_d S^2}\right)^{1/2} \tag{10}$$

where A and k are the Richardson and Boltzmann constants, respectively, T the absolute temperature, n the average number of grains across the specimen thickness, q the electron charge, ε_0 the vacuum permittivity, ε_r the relative permittivity of the metal oxide and S is the area of the electrodes [28].

Figure 7a presents the total electrical capacitance dependence with frequency for different temperatures. This result was extracted from the results shown in Fig. 6a. The capacitance is not very affected by temperature in this range which are consistent with previously reported results in polycrystalline semiconductors [29]. As it was predicted for Eq. 9, for future calculations, we will used the C_{gb} obtained at high frequencies values. In Fig. 7b, the total parallel resistance (Rp) for different temperatures as frequency function is shown. A great electrical resistance dependence with frequency can be observed for all temperatures. This phenomenon was previously explained by Ponce et at [27]. From Fig. 7b we will focus in obtaining the R_{gb} resistance that corresponds to the Rp value when frequencies tend to zero (Eq. 8). The possible origin of different resistivities of grains can be caused by the equilibrium concentration of oxygen vacancies in ABO_3 type perovskites and addition of samarium which results in loss of oxygen during sintering. This loss can be written in the Kröger-Vink notation as follows:

$O_O = 1/2O_2 + V^{\cdot\cdot}{}_O + 2e^-$.

The electrons released in the above reaction may be captured by Fe^{3+} leading to the formation of Fe^{2+}. This leads to hopping of electrons among the two different valence states, which increases conductivity of the grains. During cooling down period after sintering, the reverse reaction occurs. However due to insufficient time available during cooling, the reoxidation occurs preferentially at grain boundaries only. Thus, grain boundaries regain their insulating character, while the grains remain more or less semiconducting. The grain boundaries thus act as barriers against the hopping electrons, which pile up against them leading to space charge polarization. A similar space charge polarization occurs at the electrode-grain interface. These space charge polarization processes are responsible for the extremely large value of dielectric permittivity at very low and medium frequencies. However, at high frequencies the space charge polarizations are not able to contribute.

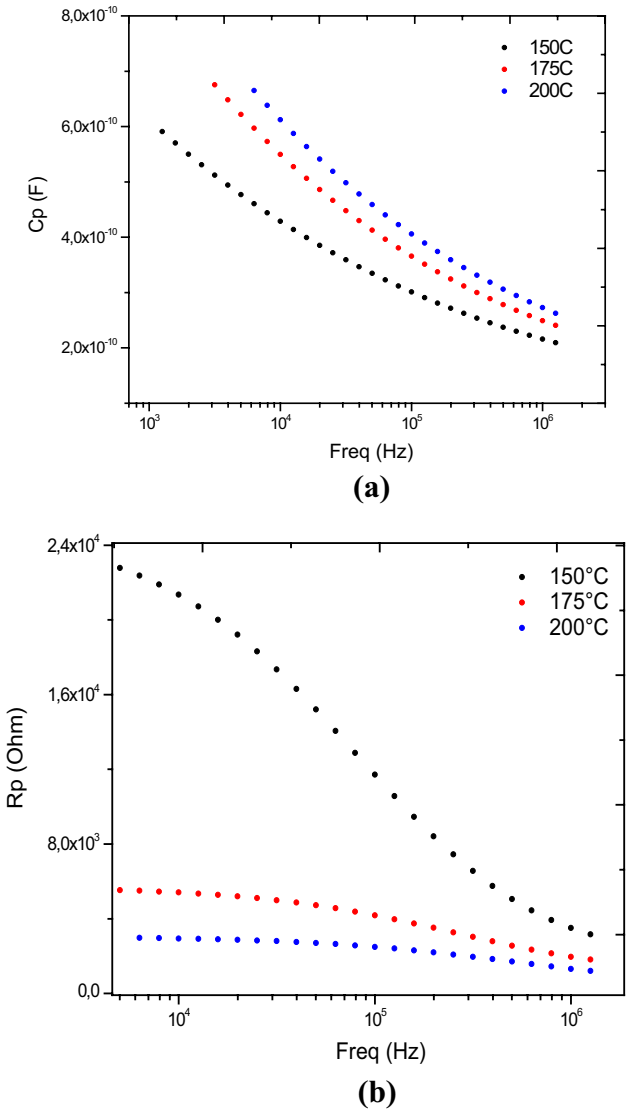

Fig. 7 **a** Total electrical capacitance and **b** total parallel resistance dependence with frequency for different temperatures of the LFO:Sm thin films deposited on Pt/Ti/SiO_2/Si(100) substrates annealed at 500 °C for 2 h film with temperature

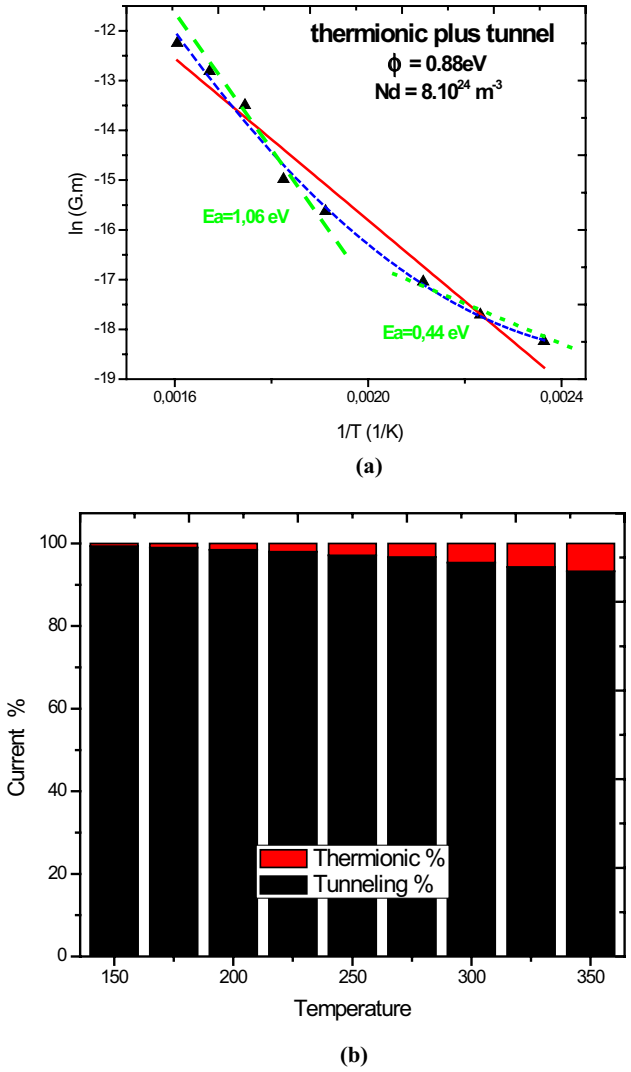

Fig. 8 **a** Arrhenius curve and **b** tunneling and thermionic behaviors for the LFO:Sm thin films deposited on Pt/Ti/SiO_2/Si(100) substrates annealed at 500 °C for 2 h film with temperature

From IS studies we deduce that the grain boundary resistance (R_{gb}) decreases as a function of temperature in the range between 150 and 200 °C. In order to study the electrical behavior versus temperature, further measurements were realized from 150 to 300 °C using four points method. In Fig. 8a the total current density is plotted as a function of temperature. The total current density over and through a barrier can be calculated as:

$$J = \frac{AT}{k}\int_0^{V_s} f(E)P(E)dE + AT^2 \exp(-e\phi/kT) \qquad (11)$$

The first term corresponds to the tunnelling current and the second to the thermionic current, A and k are the Richardson and Boltzmann constants, and $f(E)$ is the Fermi–Dirac distribution. $P(E)$, the transmission probability for a reverse-biased Schottky barrier (which is the limiting step, as was explained by Castro et al. [16]), is given by

$$P(E) = \left\{\exp -\left[\frac{4\pi V_s}{qh}\left(\frac{m\varepsilon}{N_d}\right)^{1/2}\ln\left(1-\frac{(1-\beta)^{1/2}}{\beta^{1/2}}\right)\right]\right\} \qquad (12)$$

where m is the electron effective mass, ε the electrical permittivity ($\varepsilon_{r=}$356 for our film [Fig. 4a]), h the Planck constant and β is E/φ ..

The experimental current density (J_{exp}) can be obtained from the grain boundary resistance (Fig. 8(a)) with the following relationship:

$$J = V/SR_{gb(f\to 0)} \quad (13)$$

where V is the applied voltage during impedance spectroscopy measurements, S the block area (6.5×10^{-5} m^2) and R_{gb} the grain boundary resistance measured at low frequencies ($f\to0$). Then, a pair of N_d and φ values was used for fitting experimental values with Eqs. 10–13. The first term corresponds to the thermionic contribution while the second term to the tunneling contribution. $F(E)$ is the Fermi–Dirac distribution, $P(E)$ is the transmission probability that can be calculated by means of the Wentzel-Kramer-Brilloin (WKB) approximation, and ξ the difference between the bottom of the conduction band and the Fermi level. The filled line in Fig. 8a shows the fitting using only thermionic conduction and dot line using thermionic plus tunneling conduction Eq. (11). As we mentioned, for the sake of simplicity, we adopted a simple single parabolic Schottky barrier with singly ionized donors and with the obtained Nd value, the tunneling conduction cannot be neglected in this material. Interestingly, the tunneling current is dominant along the whole temperature range measured and presents a characteristic concavity as a function of 1/T as experiments show (Fig. 8a, b). Then, assuming an Arrhenius relation with tunneling currents incorporation the effective activation energy could be determined to be $E_1=0.88$ eV. It was observed that electrical resistance of the sample exponentially decreases with the rise of temperature which established that the present sample is a semiconducting type of material. Thus, the antiferromagnetic insulator (LFO) is converted into a semiconductor after the substitution of Sm in LFO. The calculated value of the mobility activation energy of the LFO:Sm film could be also provided in Fig. 8a. The presence of two linear regions with different slopes in the Arrhenius plot could suggest that the activation energy for low temperatures is influenced by the more resistive grain boundary (R_{gb}) than the grain itself (R_b) and as the higher the grain the more conductive is the film. In the temperature range studied no changes in the grain size or Nd (dopant concentration can occur). We suggest that the increasing of Nd concentration, promoted by Sm addition, play a crucial role in the tunneling conduction mechanism of orthofferites. The film exhibited a mobility activation energy of 1.06 and 0.44 eV, which was much higher than the value (of 0.20 eV) reported by Sarma et al. [30] for nanostructured LFO thin films prepared by solid state reaction. It is largely accepted in the literature [31–33] that the charge transfer occurs via the M–O–M bonds due to the exchange of the electronic state of the transition metal between M^{+4} and M^{+3}. It is worth noting that the transition metal (M) in $LaMO_3$ perovskites is present in the M^{+3} oxidation state. The increase in ρ with T demonstrated the semiconducting nature of the LFO films, while the linearity between log (ρ) and 1000/T indicated that the mobility was thermally activated, as expected for small polaron hopping. Therefore, the conduction occurred by thermally activated jumping of holes from M^{4+} to nearby M^{3+} via the intermediate oxide ions. It has also been reported [34] that the successive jump of the hole along the (M^{4+}–O^{2-}–M^{3+}) chain is slightly influenced by the Coulomb repulsion interaction because of the presence of La^{3+}.

Magnetization (M) versus field (H) loops were recorded at 27 °C (Fig. 9). The magnetization of the film was observed with a remnant magnetization of 7.7 emu g^{-1}. Thus, the magnetization of film has been substantially enhanced which can be attributed to the modified antiferromagnetic (AFM) interaction due to samarium substituted orthoferrites. The spins of Fe^{3+} ions are aligned antiferromagnetically through a strong superexchange interaction as the angle Fe^{3+}–O^{2-}–Fe^{3+} is 180°. In LFO:Sm, Fe^{3+} ions have a distorted octahedral local environment and the distortion causes a tilting of the octahedron from the direction of c-axis. The angle of tilting depends on the ionic diameter of the A-cation. Thus, any change of size normally modifies the Fe^{3+}–O^{2-}–Fe^{3+} superexchange angle and when we substituted Sm^{3+} in place of La^{3+}, the effective size of the A-cation decreases as the ionic radius of Sm^{3+} (0.96 Å) is smaller than that of La^{3+}(1.06 Å). For this, superexchange angle is changed and consequently, the strength of the superexchange interaction is also modified, this would lead to an enhancement of magnetization. In this study, the magnetization of the LFO:Sm films non-linearly increased with the applied magnetic field, which is typical of ferri/ferromagnetic behavior where the magnetization slowly

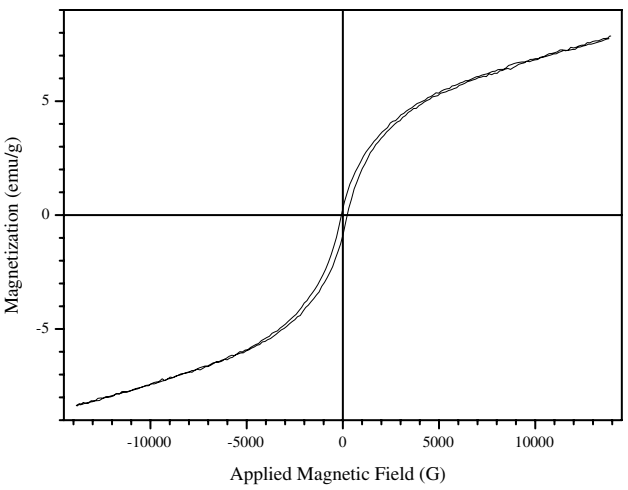

Fig. 9 Field dependencies of the magnetization obtained for the LFO:Sm thin films deposited on Pt/Ti/SiO_2/Si(100) substrates annealed at 500 °C for 2 h

approaches saturation. This behavior ruled out the presence of any dominating paramagnetic particles in the sample.

The ferroelectric hysteresis loop observed at 50 Hz of the sample is shown in Fig. 10a. The loop tracer can observe the ferroelectric loop for sample having resistance more than 200 kΩ. The resistivity of the LFO:Sm films is moderate behaving as a wide-gap semiconductor. For this it is possible to observe the ferroelectric loop by the tracer with maximum value of applied electric field (~5 kV cm^{-1}). At RT, the sample shows typical ferroelectric loop with the values of saturation polarization (Ps), remnant polarization (Pr) and the electric coercivity (Ec) are 2.55, 0.8504 μC cm^{-2} and 8.2 kV cm^{-1}, respectively. The observed loop clearly indicate the ferroelectric ordering of dipole moment configuration due to spontaneous polarization of the sample. Thus it is established that the present sample is in a state where both types of electric and magnetic orderings are present. The ferroelectric behaviour of our film at RT is also confirmed by its capacitance- voltage (*C–V*) characteristic as shown in Fig. 10b. The ''butterfly'' nature of the *C–V* curve suggests a weak ferroelectric behaviour at room temperature. This nature is also observed for other multiferroic material [35–38]. The capacitance dependence on the voltage is strongly nonlinear, confirming the ferroelectric properties of the film resulting from the domain switching. The lack of symmetry in the maximum capacitance values around the zero bias axes, indicating that the films contain few movable ions or charge accumulation at the film-electrode interface.

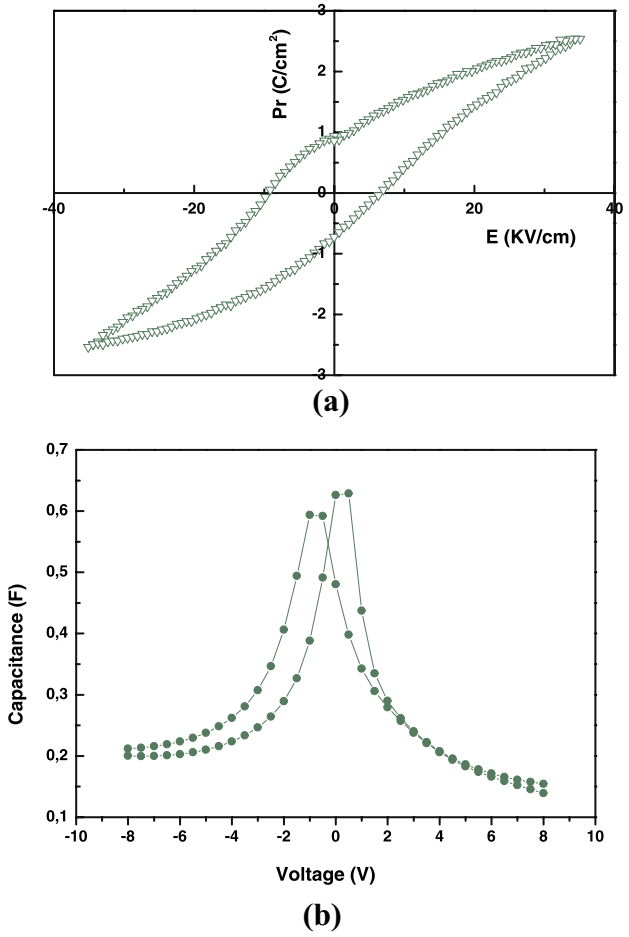

Fig. 10 **a** P–E hysteresis loops and **b** C–V characteristics for the LFO:Sm thin films deposited on Pt/Ti/SiO_2/Si(100) substrates annealed at 500 °C for 2 h

4 Conclusions

Pure perovskite Sm substituted LFO films were chemically synthesized by solution-based PPM. The non-linear magnetization curve and the ac hysteresis loops reveal the presence of dipole–dipole and/or exchange interaction in the sample suggesting a possible magnetoelectric coupling at room temperature. At room temperature the film shows typical ferroelectric loop with the values of saturation polarization (Ps), remnant polarization (Pr) and the electric coercivity (Ec) are 2.55, 0.8504 μC cm^{-2} and 8.2 kV cm^{-1}, respectively. A weak ferroelectric behaviour at room temperature is noted from *C–V* curve suggesting a new multiferroic system. The thermal variation of the resistivity shows that the sample is in a semiconducting state. The possibility to determine the magnetoelectric coupling along with the semiconducting behavior and enhanced magnetic property of the Sm substituted LFO may be useful in various applications. This finding is of particular importance to spintronic devices relying on exchange-biased nanostructures, where the possibility of domain control in antiferromagnets could open up new opportunities.

Acknowledgements This research project was financially supported by the Brazilian research funding agency FAPESP 2013/07296-2.

References

1. S.T. Shen, H.S. Weng, Comparative-study of catalytic reduction of nitric-oxide with carbon-monoxide over the $La_{1-x}Sr_xBO_3$ (B = Mn, Fe, Co, Ni) catalysts. Ind. Eng. **37**(7), 2654–2661 (1998)
2. V.V. Kharton, A.A. Yaremchenko, A.V. Kovalevsky, A.P. Viskup, E.N. Naumovich, P.F. Kerko, Perovskite-type oxides for high-temperature oxygen separation membranes. J. Membr. Sci. **163**(2), 307–317 (1999)
3. P.M. Woodward, Octaedral Tilting in Perovskites I, Geometrical Considerations. Acta Cryst. B **53**(1), 32–43 (1997)
4. M.G.A. Ranieri, M. Cilense, E.C. Aguiar, C.C. Silva, A.Z. Simões, E. Longo, Electrical behavior of chemically grown lanthanum ferrite thin films. Ceramic. Int. **42**(2), 2234–2240 (2016)

5. H Xu, X Hu, L Zhang, Generalized low-temperature synthesis of nanocrystalline rare earth orthoferrites $LnFeO_3$ (Ln = La, Pr, Nd, Sm, Eu, Gd). Cryst. Growth Des. **8**(7), 2061–2065 (2008)
6. S. Acharya, P.K. Chakrabarti, Some interesting observations on the magnetic and electric properties of Al^{3+} doped lanthanum orthoferrite ($La_{0.5}Al_{0.5}FeO_3$). Solid State Commun. **150**(1), 1234–1237 (2010)
7. E Traversa, S Matsushuma, G. Okada, Y. Sadaoka, Y. Sakai, K. Watanabe, NO_2 sensitive $LaFeO_3$, thin films prepared by R.F. Sputtering. Sens. Actuator B **661**(1), 24–25 (1995)
8. N.N. Toan, S. Saukko, V. Lantto, Gas sensing with semiconducting perovskite oxide $LaFeO_3$. Physica B **327**(2–4), 279–282 (2003)
9. R. Dogra, A.C. Junqueira, R.N. Saxena, A.W. Carbonari, J. Mestnik-Filho, M. Moralles, Hyperfine interaction measurements in $LaCrO_3$ and $LaFeO_3$ perovskites using perturbed angular correlation spectroscopy. Phys. Rev. B **63**(22), 224104 (2001)
10. A. Scholl, J. Stohr, J. Luning, J.W. Seo, J. Fomperyne, H. Siegwart, J.P. Locquet, F. Nolting, A. Anders, E.E. Fullerton, M.R. Scheinfein, H.A. Padmore, Observation of antiferromagneticdomains in epitaxial thin films. Science **287**(1), 1014–1018 (2000)
11. J. Nogues, I.K. Schuller, Exchange bias. J. Magn. Magn. Mater. **192**(2) (1999): 203–232.
12. Y. Yamada, T. Kusumori, H. Muto, Pinning effect of a $LaFeO_3$ buffer layer on the magnetization of a La_{1-x} Pb_x MnO_3 layer. Appl. Phys. Lett. **80**(8), 1409–1411 (2002)
13. D.S. Deng, X.F. Jin, Exchange bias in ferromagnetic/compensated antiferromagnetic bilayer. Phys. Rev. B **65**(1), 172402–172406 (2002)
14. S.F. Dann, D.B. Currie, M.T. Weller, M.F. Thomas, A.D. Al-Rawwas, The Effect of oxygen stoichiometry on phase relations and structure in the system $La_{1-x}Sr_xFeO_{3-\delta}$ ($0 \le x \le 1$, $0 \le \delta \le 0.5$). J. Solid State Chem. **109**(1), 134–144 (1994)
15. I. Hole, T. Tybel, J.K. Grepstad, I. Warnhus, T. Grande, K. Wiik, High temperature transport kinetics in heteroepitaxial $LaFeO_3$ thin films. Solid State Electron. **47**(1), 2279–2282 (2003)
16. N.G. Eror, H.U. Anderson, Polymeric precursor synthesis of ceramic materials, MRS Online Proc. Libr. **73**, 571 (1986)
17. S.G. Cho, P.F. Johnson Sr., R.A. Condrate, Thermal decomposition of (Sr,Ti) organic precursor during the Pechini process. J. Mater. Sci. **25**(11), 4738–4744 (1990)
18. R.S. Devan, S.B. Deshpande, B.K. Chougule, J. Phys. D **40**(1), 1864–1868 (2007)
19. M.P. Pechini, Method of preparing lead and alkaline earth titanates and niobates and coating method using the same to form a capacitor. US Pat. No **3** 330 697 (1967)
20. D. Liu, M. Wang, Preparation of $La_{1-z}Sr_zCo1\text{-}yFeyO_{3-x}$ thin films, membranes, and coatings on dense and porous substrates. J. Mater. Res. **10**(12), 3210–3221 (1995)
21. M. Okuyama, Y. Hamakawa, Preparation and basic properties of $PbTiO_3$ ferroelectric thin films and their device applications. Ferroelectrics **63**(1), 243–252 (1985)
22. G Biasotto, MGA Ranieri, C.R. Foschini, A.Z. Simões, E. Longo, J.A. Varela, M.A. Zaghete, Gas sensor applications of zinc oxide thin film grown by the polymeric precursor method. Ceram. Int. **40**(9), 14991–14996 (2014)
23. A.Z. Simões, A.H.M. Gonzalez, M.A. Zaghete, J.A. Varela, B.D. Stojanovic, Effects of annealing and viscosity on the surface roughness of PLZT thin films. Thin Solid Film. **384**(1), 132–137 (2001)
24. W.M. Zhu, Z.-H. Ye, Effects of chemical modification on the electrical properties of $0.67BiFeO_3$–$0.33PbTiO_3$ ferroelectric ceramics. Ceram. Int. **30**, 1435 (2004)
25. M. Seitz, F. Hampton, W. Richmond, Influence of chemisorbed oxygen on the ac electrical behavior of polycrystalline ZnO. Adv. Ceram. **7**, 60–70 (1983)
26. M.A. Ponce, C.M. Aldao, M.S. Castro, Effects of previous treatments on the electrical response of SnO_2-thick films exposed to a CO atmosphere. Mater. Sci. Eng. B **123**, 130–135 (2005)
27. M.A. Ponce, C.M. Aldao, M.S. Castro, Capacitance and resistance measurements of SnO_2 thick-films. J. Mater. Sci. **20**, 25–32 (2009)
28. C.R. Crowell, V.L. Rideout, Normalized thermionic-field (T-F) emission in metal-semiconductor (Schottky) barriers. Solid-State Electron. **12**, 89–105 (1969)
29. C.M. Aldao, F.J. Williams, E. Joanni, F. Schipani, M.A. Ponce, Conductivity in SnO_2 polycrystalline thick film gas sensors: tunneling electron transport and oxygen diffusion. Sens. Actuators B **193**, 428–433 (2014)
30. D.D. Sarma, N. Shanthi, S.R. Barman, N. Hamada, H. Sawada, K. Terakura, Band theory for ground-state properties and excitation spectra of Perovskite $LaMO_3$ (M = Mn, Fe, Co, Ni). Phys. Rev. Lett. **75**(6), 1126–1129 (1995)
31. N. Fujihira, T. Sei, T. Tsuchiya, Preparation and properties of highly conductive $La_{1-x}M_xMnO_{3-y}$ thin film showing magnetic effect from Sol–Gel process. J. Sol–Gel Sci. Technol. **4**(2), 135–140 (1995)
32. M. Losurdo, A. Sacchetti, P. Capezzuto, G. Bruno, L. Armelao, D. Barreca, G. Bottaro, A. Gasparotto, C. Maragno, E. Tondello, Optical and electrical properties of nanostructured $LaCoO_3$ thin films. Appl. Phys. Lett. **87**(6), 061909–061911 (2005)
33. K. Gaur, S.C. Verma, H.B. Lal, Defects and electrical conduction in mixed lanthanum transition metal oxides. J. Mater. Sci. **23**(5), 1725–1728 (1988)
34. M.V. Patrakeev, J.A. Bahteeva, E.B. Mitberg, I.A. Leonidova, V.L. Kozhevnikov, K.R. Poeppelmeier, Electron/hole and ion transport in $La_{1-x}Sr_xFeO_{3-\delta}$. J. Solid State Chem. **172**(1), 219–231 (2003)
35. C.R. Serrao, A.K. Kundu, S.B. Krupanidhi, UV Waghmare, Rao CNR Biferroic $YCrO_3$, Phys. Rev. B **72**(1), 220101(R) (2005)
36. J. Ross MacDonald ed. *Impedance Spectroscopy, Emphasizing Solid Materials and Systems*, (Wiley & Sons, New York, 1987)
37. J. Fleig, The influence of non-ideal microstructures on the analysis of grain boundary impedances. Solid State Ionics **131**, 117–127 (2000)
38. H.L. Tuller, Ionic conduction in nanocrystalline materials. Solid State Ionics **131**, 143–157 (2000)